International Journal of Pharmaceutics 407 (2011) 12–20

Contents lists available at ScienceDirect

International Journal of Pharmaceutics

journal homepage: www.elsevier.com/locate/ijpharm

Computational and experimental investigation of needle-shaped crystal breakage

Zdeněk Grof[a], Carl M. Schoellhammer[b], Pavol Rajniak[b], František Štěpánek[a,*]

[a] Department of Chemical Engineering, Institute of Chemical Technology, Technická 5 166 28 Prague, Czech Republic
[b] Merck & Co., Inc., West Point, PA, USA

ARTICLE INFO

Article history:
Received 14 June 2010
Accepted 29 December 2010
Available online 11 January 2011

Keywords:
DEM
Population balance modeling
Fragmentation
Daughter length distribution
Breakage kernel

ABSTRACT

Needle-shaped crystals are a common occurrence in many pharmaceutical and fine chemicals processes. Even if the particle size distribution (PSD) obtained in a crystallization step can be controlled by the crystal growth kinetics and hydrodynamic conditions, further fluid–solid separation steps such as filtration, filter washing, drying, and subsequent solids handling can often lead to uncontrolled changes in the PSD due to breakage. In this contribution we present a combined computational and experimental methodology for determining the breakage kernel and the daughter distribution functions of needle-shaped crystals, and for population balance modeling of their breakage. A discrete element model (DEM) of needle-shaped particle breakage was first used in order to find out the appropriate types of the breakage kernel and the daughter distribution functions. A population balance model of breakage was then formulated and used in conjunction with experimental data in order to determine the material-specific parameters appearing in the breakage functions. Quantitative agreement between simulation and experiment has been obtained.

1. Introduction

Needle-shaped crystals (crystals with a large aspect ratio) are commonly encountered in pharmaceutical processes. While the particle size distribution (PSD) can nowadays be controlled relatively precisely in the crystallization step by adjusting the supersaturation, seeding, and hydrodynamic conditions in the crystallizer (Yu et al., 2007), further downstream fluid-solid separation steps such as filtration, filter washing, drying, and subsequent solids handling can often lead to uncontrolled changes in the PSD due to attrition and breakage (Müller et al., 2006; Kalman, 2000). The effect of breakage on the particle size distribution can be described by population balances (Hill and Ng, 1997; Kostoglou, 2007). For population balance models of breakage to be effective, two material- and stress-field specific functions need to be known: the breakage kernel (selection function) and the daughter distribution function (breakage function) (Austin, 1971; Kelly and Spottiswood, 1990). The breakage kernel determines the breakage rate of particles from each size fraction, while the daughter distribution function describes the size distribution of daughter particles (fragments) that are formed once a particle of a given size does break.

Although methodologies for experimental determination of the breakage kernel and daughter distribution functions are known (Gupta et al., 1981), they either require a relatively large number of experiments or the solution of an inverse problem (Sathyagal et al., 1995). An alternative approach is based on trying to determine the functions theoretically (Hill, 2004) or computationally by detailed mechanistic modeling of the breakage of single particles (Khanal et al., 2005) or particle ensembles (Bobet et al., 2009; Ketterhagen et al., 2008). Grof et al. (2007) recently demonstrated the feasibility of detailed numerical simulation of the breakage of needle-shaped particles within a random packed bed subjected to uni-directional compaction, using the discrete element method (DEM). Elongated particles with a chosen aspect ratio have been created by linking individual spherical discrete elements by rigid bonds, characterized by a given bending stiffness and ultimate bending strength. A randomly packed bed of these elongated particles has been formed and gradually compressed between two infinite parallel solid planes. The particle size distribution as a function of the compaction ratio has been studied while systematically varying the individual particle strength, the initial particle length, and its distribution.

The aim of the present work is to develop and validate a novel methodology for the determination of the breakage kernel and daughter distribution functions, based on the combination of computational and experimental techniques. The methodology consists of four parts: *(i)* the DEM simulation of needle-shaped particle breakage under uni-axial compaction as described in (Grof et al., 2007); *(ii)* post-processing of the DEM simulation outputs using population balance models and explicit evaluation of the appropriate types of the breakage functions; *(iii)* experimental study of the breakage of real needle-shaped crystals under uni-axial

* Corresponding author. Tel.: +420 220 443 236; fax: +420 220 444 320.
E-mail address: Frantisek.Stepanek@vscht.cz (F. Štěpánek).

0378-5173/$ – see front matter © 2011 Elsevier B.V. All rights reserved.
doi:10.1016/j.ijpharm.2010.12.031

Nomenclature

a	compression parameter (dimensionless)
A	die cross-section area (m^2)
C	span of Gaussian function (dimensionless)
E	specific energy input (J/kg)
F	compaction force (N)
$f(y)$	compression function ($m\,s^{-2}$)
$g(F)$	alternative form of compression function (m/kg)
h	bed height (m)
$k(L_i)$	breakage kernel (kg/J)
k_0	breakage constant (dimensionless)
L_i	length of a crystal from the ith size class (m)
L_0	characteristic length (m)
m	sample mass (kg)
N	number of size classes (dimensionless)
n_i	number concentration of crystals from the ith size class (kg^{-1})
P	compaction pressure (Pa)
r_i	breakage rate (J^{-1})
$S_m(L_i)$	breakage probability (dimensionless)
U	objective function (kg^{-2})
y	relative piston position (dimensionless)
z	piston travel distance (m)

Greek letters

$\beta(i,j)$	daughter distribution function (dimensionless)
$\beta'(x)$	transformed (universal) daughter distribution function (dimensionless)
γ	breakage exponent (dimensionless)

compaction; *(iv)* fitting of the population balance models to the experimental data and evaluation of the material-specific parameters in the breakage functions.

2. Population balance model

When applying the rigorous population balance model (Vanni, 2000) to needle-shaped crystals we assume that the crystals are linear aggregates of primary particles (or "monomers") of equal size. Such a description is consistent with the multi-element particle model (Favier et al., 1999; Grof et al., 2007) used for the representation of elongated (needle-shaped) particles or crystals. This assumption makes it possible to correlate the length L_i of a crystal with the number of primary particles i that form it as:

$$L_i \approx i. \tag{1}$$

The particle size distribution is then a discrete function, whose values n_i, $i = 1, \ldots, N$ are the number concentrations of the particles consisting of i monomers and N is the number of size classes.

Theoretical treatments of Weichert (1992), Fuerstenau et al. (1996, 2004), lead to expressing the population balance equations for the breakage under uni-axial compression in terms of the specific energy expended rather than in grinding time as follows

$$\frac{dn_i}{dE} = -r_i + \sum_{j=i+1}^{N} \beta_{ij} r_j. \tag{2}$$

The first term on the right side of Eq. (2) is the rate of death of particles i to generate smaller fragments, while the second one is the birth of particles i due to rupture of larger particles.

The specific energy input E can be equated with the work of compression per unit feed mass (Fuerstenau et al., 1996)

$$E \approx \frac{APz}{m} = \frac{Fz}{m}, \tag{3}$$

where A is the die cross-sectional area, P is the compaction pressure, F is the compaction force, m is the sample mass which is proportional to the initial bed height

$$m \approx h_0 \tag{4}$$

and z is the piston travel distance which may be expressed in terms of h_0 and h, the initial and instantaneous bed heights

$$z = h_0 - h. \tag{5}$$

Kawakita and Lüdde (1971) listed 15 equations of compaction that relate pressure with volume (or bed height). For example the Kawakita piston compression equation has the form

$$\frac{z}{m} \approx y = \frac{h_0 - h}{h_0} = \frac{abP}{1 + bP} = \frac{acF}{1 + cF} \tag{6}$$

or

$$P = \frac{y}{b(a - y)}, \tag{7}$$

where y is the degree of volume reduction (or relative piston position) and a and b are parameters characterizing the powder. The parameter a is equal to the initial porosity in the case of piston compression. By combining relations (3)–(7) and lumping all proportionality constants, the specific energy may be expressed as

$$E \approx Py \approx \frac{y^2}{a - y} \tag{8}$$

and consequently

$$dE \approx \frac{2ay - y^2}{(a - y)^2} dy = f(y)\,dy. \tag{9}$$

Breakup is usually a first order process with respect to particle concentration, since it generally depends on the local stress field acting on the particles. It is convenient to express the death rate as

$$r_i = k(L_i) n_i, \tag{10}$$

where $k(L_i)$ is the breakage kernel. There is a strong dependence of the breakage kernel on particle size, L_i. Different breakage kernels are summarized in (Vanni, 2000; Rajniak et al., 2008).

Finally, introducing (9) and (10) into the rigorous population balances (2) and lumping different proportionality factors together we get the population balance equations in terms of the relative piston position y

$$\frac{dn_i}{dy} = -f(y)k(L_i)n_i + \sum_{j=i+1}^{N} \beta_{ij} f(y) k(L_j) n_j \tag{11}$$

with $f(y)$ defined by Eq. (9).

There exist many different fragment (daughter) distribution functions β_{ij} defining the number of daughter fragments in class i produced upon breakup of a mother particle j (Vanni, 2000; Rajniak et al., 2008). Here we have considered only the formation of two fragments during every breakage event, i.e. corresponding binary breakage distribution functions are normalized with respect to condition (12)

$$\sum_{i=1}^{j-1} \beta_{ij} = 2. \tag{12}$$

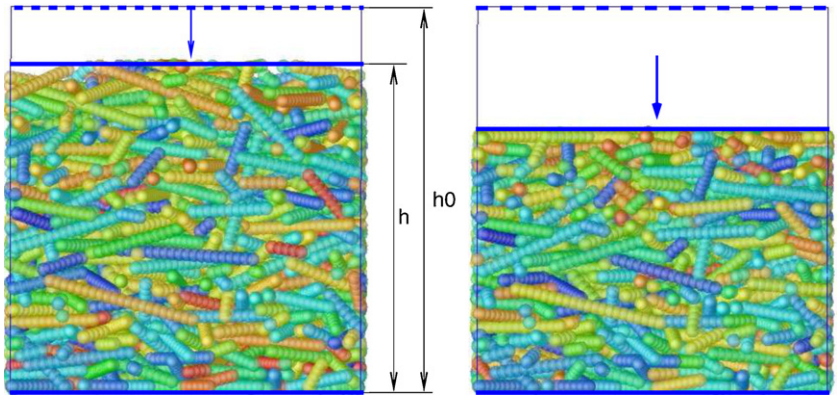

Fig. 1. Simulation setup for discrete element modelling of uniaxial compression and breakage of needle-shape particles.

An alternative form of the model equations are based on expression (6) with the compression force F as the independent variable. For the specific energy input we can write

$$E \approx Fy \approx \frac{cF^2}{1+cF} \tag{13}$$

and consequently

$$\mathrm{d}E \approx \frac{2F+cF^2}{(1+cF)^2}\mathrm{d}F = g(F)\,\mathrm{d}F. \tag{14}$$

The alternative population balance equations then have the following form

$$\frac{\mathrm{d}n_i}{\mathrm{d}F} = -g(F)k(L_i)n_i + \sum_{j=i+1}^{N} \beta_{ij} g(F)k(L_j)n_j. \tag{15}$$

In the next chapter we will discuss how the discrete element methodology helps elucidate appropriate expressions for the breakage kernel and daughter distribution functions.

3. Discrete element method

3.1. Simulation of the compression and breakage of a layer of particles

A methodology based on the discrete element method (Cundall and Strack, 1979) modified to treat non-spherical particles by the multi-element model (Favier et al., 1999) has been used to simulate the movement and breakage of individual needle-shaped particles. The magnitude and the location of contact forces at each particle determine the load on the particle. Particles are treated as loaded beams in order to calculate bending and shear stresses along the particle. When a set threshold value anywhere along a particle is exceeded the particle breaks into two daughter particles at the point of maximum stress. A full description of the algorithm has been given in our earlier work (Grof et al., 2007).

In order to determine the breakage kernel and the daughter distribution function for a sample of needle-shaped particles, the computational breakage experiment has been carried out in the following way. First, a population of 800 particles with a specified size distribution was generated inside the computational box with periodic boundary conditions in the direction of the x- and y-axes and a fixed wall perpendicular to the xy-plane (at the bottom boundary of the box). The particles were allowed to settle down due to gravitational forces in the direction of the z-axis thus forming the initial random packing desired. A second wall parallel with the xy-plane was then placed above the packing and compression was simulated by a stepwise movement of this piston (cf. Fig. 1). After each step of the piston, the particles were allowed to move and rearrange in the packed layer until a static state was achieved. The stress on every particle was then calculated and particle breakage carried out where required.

Every breakage event encountered during the simulated compression experiment has been recorded and the following data collected: *(i)* the relative piston position (compression ratio) $y = (h_0 - h)/h_0$, where h and h_0 are the current and the initial packing heights, respectively, determined by the piston position; *(ii)* the length L_i of the (mother) particle before breakage; *(iii)* if the particle broke during a given compression step, the length of the shorter daughter particle. The results collected from simulated compression experiments of five different particle packings are shown in Fig. 2, where each curve represents the particle length distribution at a given compression ratio y. The error bars indicate the standard deviations due to the five different random realizations of the initial particle packing. The gradual particle breakage is clearly demonstrated as the particle size distribution shifts towards shorter particles and the number of longer particles diminishes with increasing y.

3.2. Breakage kernel

The breakage kernel is obtained by post-processing of the breakage events recorded during the computational experiment. The breakage events were first grouped into M intervals $m = 0, \ldots, M$ according to the compression ratio y for which they occurred. A

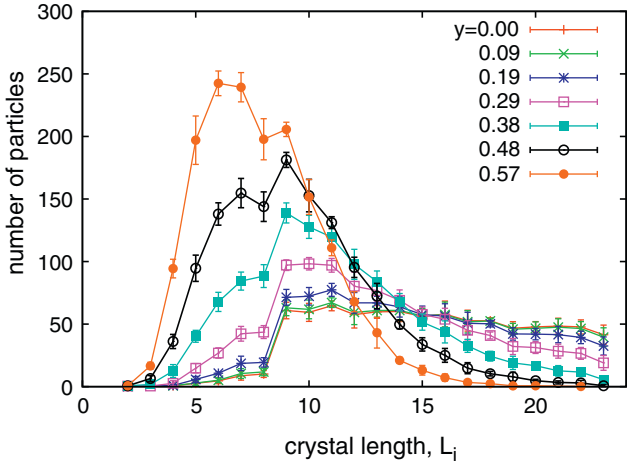

Fig. 2. Evolution of PSD with compression ratio y in a DEM simulation. The error bars represent the standard deviation obtained by compounding the results of compressing five different random realizations of the initial particle packings.

breakage probability $S_m(L_i)$ is defined as the probability that a particle of length L_i that was originally present in the system at compression ratio y_m disappeared from the system (i.e., it was broken) at some stage while the compression ratio y was in the range $\langle y_m\,;y_{m+1}\rangle$. This breakage probability was calculated according to

$$S_m(L_i) = 1 - \frac{n_i(y_{m+1})}{n_i(y_m)}, \tag{16}$$

where $n_i(y_m)$ is the number of particles of length L_i present in the system at compression ratio y_m and $n_i(y_{m+1})$ is the number of such particles still "surviving" in the system at y_{m+1}. Note that any newly formed particles of length L_i are not counted into $n_i(y_{m+1})$ when evaluating $S_m(L_i)$.

Let us derive the relation between the breakage probability $S_m(L_i)$ and the breakage kernel $k(L_i)$, introduced above. From Eq. (11), the number of particles undergoing breakage during the interval $\langle y_m\,;y_{m+1}\rangle$ is

$$\Delta n_i = (n_i(y_m) - n_i(y_{m+1})) = k(L_i)f(\overline{y})\Delta y\overline{n_i}. \tag{17}$$

Assuming that $\overline{n_i}\doteq n_i(y_m)$ and substituting Eq. (17) into the relation for S_m (16) one obtains

$$S_m(L_i) = k(L_i)f(\overline{y})(y_{m+1} - y_m). \tag{18}$$

The breakage probability $S_m(L_i)$ evaluated from DEM simulations is shown in Fig. 3a. Then, as shown in Fig. 3b and c the curves can be fitted by the sigmoidal and power-law functions of the form:

$$S_m(L_i) = \frac{1}{1+\exp(-\gamma_m(L_i - L_{0,m}))} \text{ and} \tag{19a}$$

$$S_m(L_i) = \alpha(L_i - L_{0,m})^{\gamma_m}. \tag{19b}$$

It can be seen from Fig. 3b and c that the sigmoidal function provides a better fit of the breakage probability obtained by DEM simulation than the power law function. In particular, the sigmoidal function satisfies the property that in the limit for large particles, the breakage probability approaches unity, while the power law function diverges. Using a single parameter α for the entire range of the compression ratio, the power law is able to fit the DEM data well only at small compression ratio y, but fails for the two curves at $y > 0.48$. A better fit could be obtained by using three parameters in the power law, i.e., by allowing the value of α to depend on the compression ratio. On the other hand, the sigmoidal function is able to fit the data well over the entire range of y with only two adjustable parameters.

3.3. Daughter distribution function

To evaluate the daughter distribution function $\beta(i,j)$, the entire set of breakage events recorded for compression in the range $\langle y_0\,;y_M\rangle$ was used. Unlike the breakage probability $S_m(L_i)$, there is no reason to assume that the daughter distribution $\beta(i,j)$ would depend on the compression ratio. Moreover, the larger number of breakage events analyzed reduces the variations of data points in the evaluated function. Let $D_{i,j}$ be the number of breakage events where the particle of length j breaks into particles of length i and $j-i$, respectively, and let $i<j-i$ (i.e. the shorter of the two fragments is given the index i). Then the points in the the daughter distribution $\beta(i,j)$ are calculated as

$$\beta(i,j) = \frac{D_{i,j}}{\sum_{k=1}^{j/2} D_{k,j}}, \quad i = 1,\ldots,j/2 \tag{20a}$$

and the other half can be completed employing the symmetry of the distribution

$$\beta(i,j) = \beta(j-i,j) \quad i = j/2,\ldots,j. \tag{20b}$$

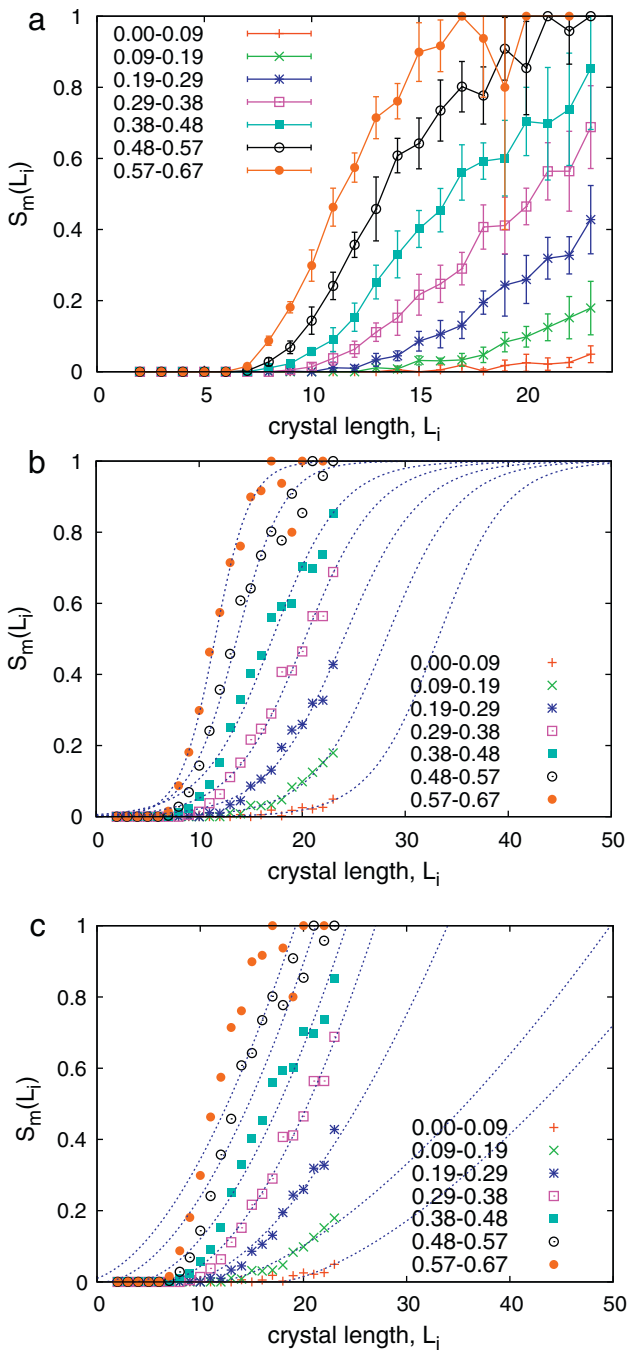

Fig. 3. Compression-dependent breakage kernel from DEM simulation: (a) computation data with error bars representing the standard deviation obtained from five simulation runs, (b) fit of data by a sigmoidal function (19a), (c) fit of data by a power-law function (19b).

If the breakage is self-similar, then a single daughter distribution function $\beta'(x)$, where $x = i/j$, characterizes the breakage of mother particles of any length j. For binary breakage (two fragments from a single breakage event) the daughter distribution functions are normalized to 2:

$$\sum_{i=1}^{j}\beta(i,j) = \int_0^1 \beta'(x)\,\mathrm{d}x = 2. \tag{21}$$

The normalized daughter distribution $\beta'(x)$ obtained from the DEM simulations is shown in Fig. 4. Based on DEM simulation data analysis, it has been confirmed the breakage is indeed self-similar,

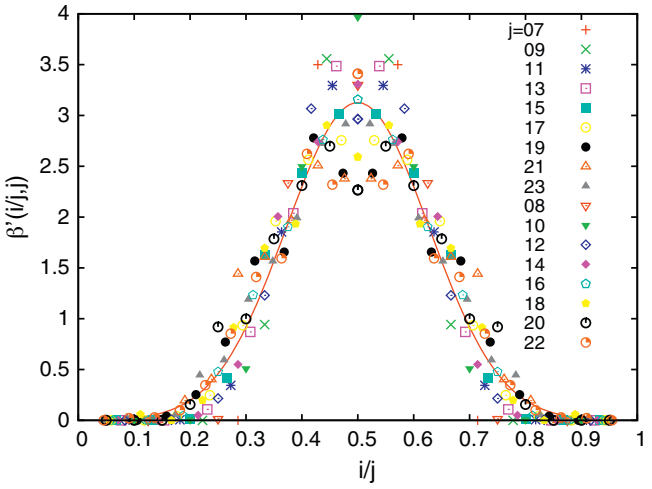

Fig. 4. Normalized (universal) daughter distribution $\beta'(i|j,j)$. Mean values evaluated from five different random sample realizations are displayed and fitted by a Gaussian function (22).

as breakage functions for particles of different lengths superimpose on a single master curve that can be fitted by the Gaussian function

$$\beta'(x) = \frac{2}{\sigma\sqrt{2\pi}} \exp\left(-\frac{(x-\mu)^2}{2\sigma^2}\right) \tag{22}$$

with parameters $\mu = 0.5$ and $\sigma = 0.1276 \pm 0.0016$. Therefore, the daughter distribution for mother particle of length L_j is

$$\beta(i,j) = \frac{2}{j\sigma\sqrt{2\pi}} \exp\left(-\frac{(i-j/2)^2}{2(j\sigma)^2}\right), \tag{23}$$

where the linear dependence of distribution width on mother particle length is described by the proportional parameter σ.

4. Fitting of computational DEM results by PBM

In the previous section, it has been demonstrated that the two *a priory* unknown functions required in the population balance equations (11) – i.e. the breakage kernel $f(y)k(L_i)$ and the daughter distribution β_{ij} – can be directly evaluated by post-processing of DEM simulation results. There are two ways of utilizing the results from Sections 3.2 and 3.3. The breakage kernel and the daughter distribution can be constructed directly by finding an arbitrary function able to provide a good approximation of $f(y)k(L_i)$ or β_{ij} data, then performing a least-square regression of those data and evaluating the function's parameters. The other option is to use DEM results for proposing suitable shapes of the breakage kernel and daughter distribution functions. The parameters of those functions are then found by optimization to achieve the best match of particle size distribution predicted by PBM with DEM result. The latter method will be demonstrated in this section. Its main advantage is that it only requires the PSD at several compression ratios as its input, which is also the format in which experimental data are available (unlike in DEM simulations, the recording and post-processing of single breakage events is not feasible in a real experiment). Thus, the estimation method for PBM functions and parameters can be the same, but the input data can originate either from a computational or from a physical experiment.

The key observations from the evaluation of the DEM simulations discussed in section 3 are that the breakage kernels can be more or less successfully fitted by power-law and sigmoidal functions

$$k(L_i) = k_0(L_i - L_0)^{\gamma} \tag{24a}$$

$$k(L_i) = \frac{k_0}{1 + \exp(\gamma(L_i - L_0))} \tag{24b}$$

and that the daughter distribution function is self-similar and can be fitted by the Gaussian function. Let us now find the values of parameters appearing in the breakage kernel and daughter distribution function by fitting a population balance model (PBM) introduced in Section 2 to the DEM results.

After introducing the power-law compression breakage kernel (24a) into the PB equations (11) with relative piston position y as the independent variable, the following final form of PBE for each size class i is

$$\frac{dn_i}{dy} = k_0 \frac{2ay - y^2}{(a-y)^2} \left(-(L_i - L_0)^{\gamma} n_i + \sum_{j=i+1}^{N} \beta_{ij} (L_j - L_0)^{\gamma} n_j \right) \tag{25}$$

and similarly also for the sigmoidal breakage kernel (24b). The parameters β_{ij} are calculated from the Gaussian daughter distribution function

$$\beta_{ij} \approx \exp\left(-\frac{(i-j/2)^2}{(NC)^2}\right). \tag{26}$$

There are five adjustable parameters in the model equations (25) and (26), i.e., the compression parameter a, the breakage constant k_0, the breakage exponent γ, the characteristic length L_0 and span of the Gaussian daughter distribution function C.

A customized (Compaq Visual Fortran) version of the DIRECT optimization algorithm (Perttunen et al., 1993; Bjorkmann and Holmstrom, 1999) was employed for finding the global minimum of the objective function U

$$U = \sum_{m=1}^{7} \sum_{i=1}^{N} \left(n_i^{\exp}(y_m) - n_i^{\mathrm{cal}}(y_m)\right)^2 \tag{27}$$

constrained by the population balances (25). $n_i(y_m)$ is the calculated or experimental number concentration of crystals of the class i at the piston position y_m.

The optimized parameter values and the corresponding objective functions are compared in Table 1 and a graphical comparison with the DEM simulation results is shown in Fig. 5. Please note that the DEM data in Fig. 5 are the same as those in Fig. 2 but they are shown in the cumulative rather than differential form for clarity. It can be concluded that the fit is visually satisfactory for both the power-law and sigmoidal function. The objective function at optimum ($U = 0.0113$) is slightly better when employing the power-law breakage kernel than for the sigmoidal kernel ($U = 0.0168$). A possible reason is that the functions calculated from DEM results (Fig. 3) have a sigmoidal shape only for the highest compressions (at piston positions y_6 and y_7) as it was already discussed in relation to Fig. 3. It is interesting to note that the value of the compression

Table 1
Fitting of the DEM results by PBM.

Breakage kernel, $f(y)k(L_i)$	$f(y)$	a	k_0	γ	L_0	C	U
$f(y)(L_i - L_0)^{\gamma}$	Eq. (9)	0.730	0.0185	1.75	6	0.081	0.0113
$\frac{f(y)}{1+\exp(-\gamma(L_i - L_0))}$	Eq. (9)	0.733	1.35	0.667	12.7	0.07	0.0168

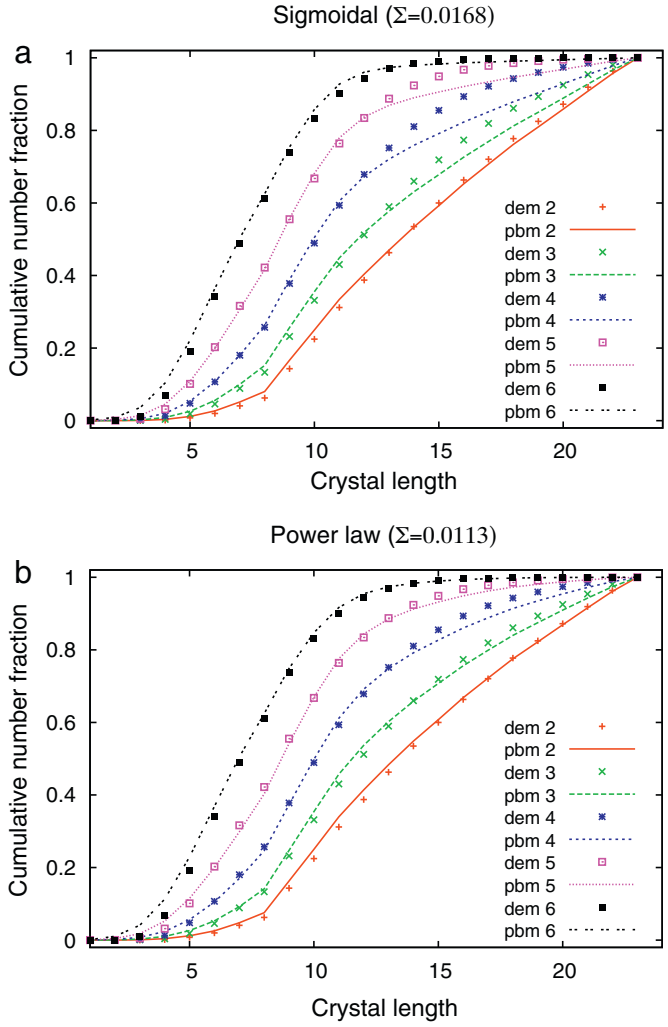

Fig. 5. Comparison of size distribution obtained by the DEM simulation with the distribution calculated by PB model using (a) sigmoidal and (b) power-law form of the breakage kernel in the PB equations.

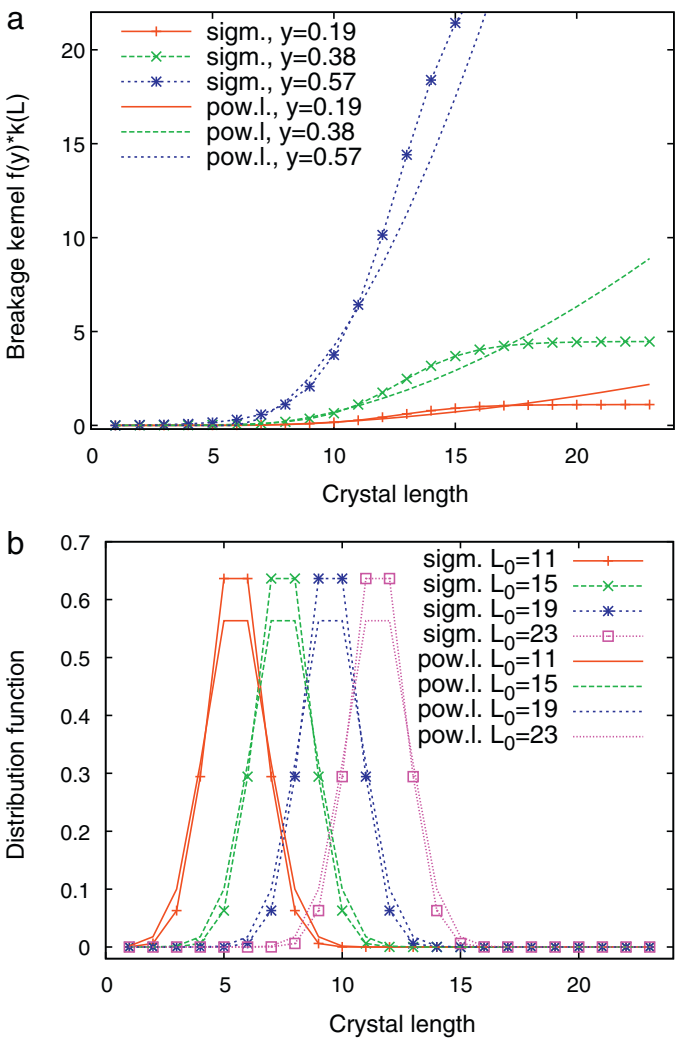

Fig. 6. (a) The breakage kernel and (b) the daughter distribution functions in PB equations.

parameter is almost exactly the same for both kernels (a = 0.730 vs. 0.733) and is also close to the theoretical value of the initial porosity (ε_0 = 0.77) of the needle-shape crystals in the DEM simulation sample. Also the optimum span of the self-similar Gaussian daughter distribution function is comparable for both cases as it is also illustrated in Fig. 6b. The values of other optimum parameters are different because of the different mathematical expressions used for the breakage kernels.

5. Experimental study

The experimental breakage study was carried out using crystals of a pharmaceutical compound, a white crystalline solid composed of needle-shaped particles with a mean length of approximately 31 μm and an aspect ratio of 70. These crystals were chosen for this study because their size, shape and fragility are characteristic of typical materials encountered during the process development for active pharmaceutical ingredients (APIs).

The uni-axial compaction breakage experiment was carried out as follows. First, approximately 4 mg of the powder was weighed out and loaded into a 3.8 mm diameter stainless steel die. The top punch was placed gently into the die, resting on top of the sample. An automatic texture analyzer (Stable Micro Systems TA.XT2i) was then used to apply force on the sample and measure the force-displacement curve. Each sample was compacted once under a normal load of 200, 400, 800, and 1600 g (corresponding to pressures of 0.173, 0.346, 0.692 and 1.381 MPa, respectively) with the punch displacement rate set to 0.1 mm/s. Once the specified compression load was achieved, the upper punch was immediately raised away from the sample. An example of typical force–displacement curves obtained in the course of a single experiment is shown in Fig. 7.

Once the sample had been compacted, it was gently pushed out of the die and into a sonication vial where it was dispersed in Isopar G with 0.25% Lecithin, which the sample is not soluble in. The sample was sonicated for 30 s intervals until the pellet was evenly dispersed in the fluid. A microscope slide was cleaned, and using a dropper, one drop was placed on the slide from approximately 1 cm above the slide. The liquid was allowed to air-dry and then the sample was visualized using an Olympus SZX16 Stereo Microscope. Ten images were randomly selected from across the width of the slide and analyzed using the Image Pro Plus software. The length, aspect ratio, and projected area were the three statistics taken from each image. From this data, particle size distributions were created and compared to an uncompacted standard.

Representative images of samples compacted to various forces can be seen in Fig. 8. The evolution of the PSD with increasing compaction load is shown in Fig. 9 and the mean particle size as a function of the compaction load is summarized in Fig. 10. It can

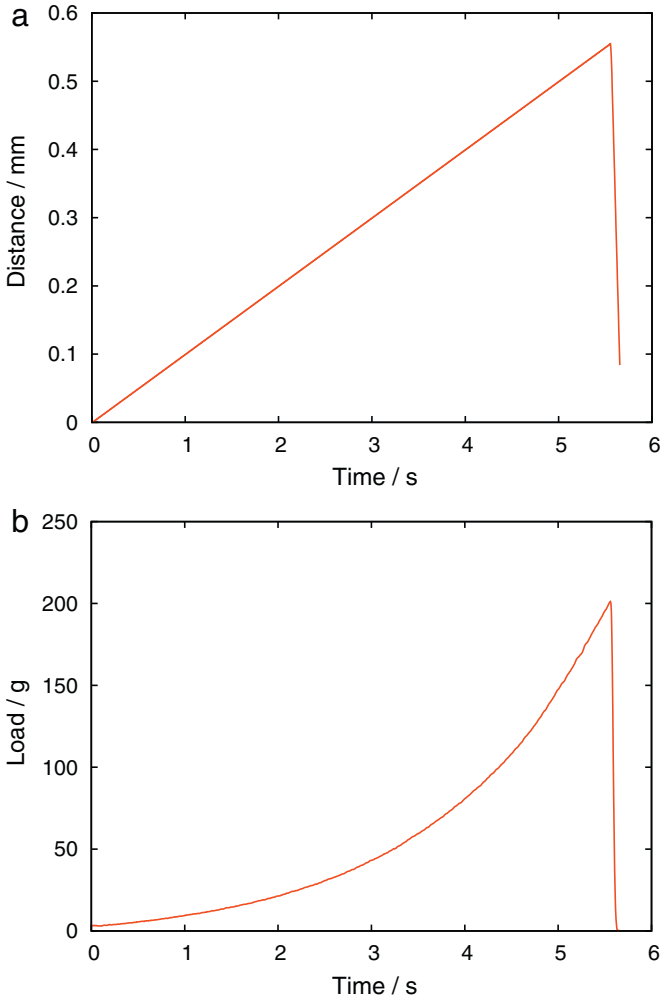

Fig. 7. Example of force displacement curves obtained in the 200 g load experiment.

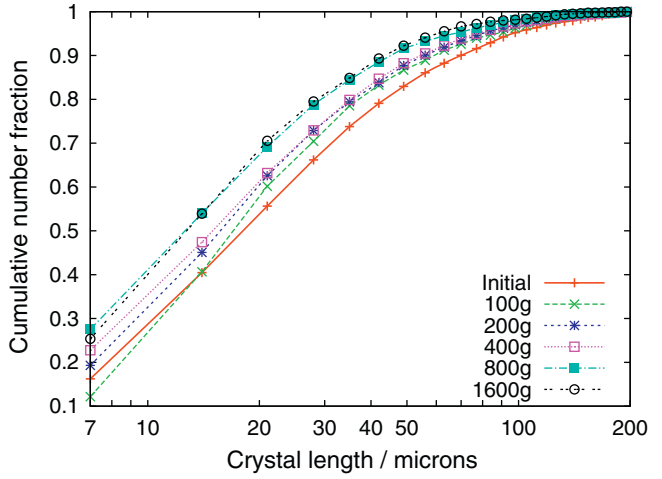

Fig. 9. Experimental PSD at different breakage forces evaluated from image analysis.

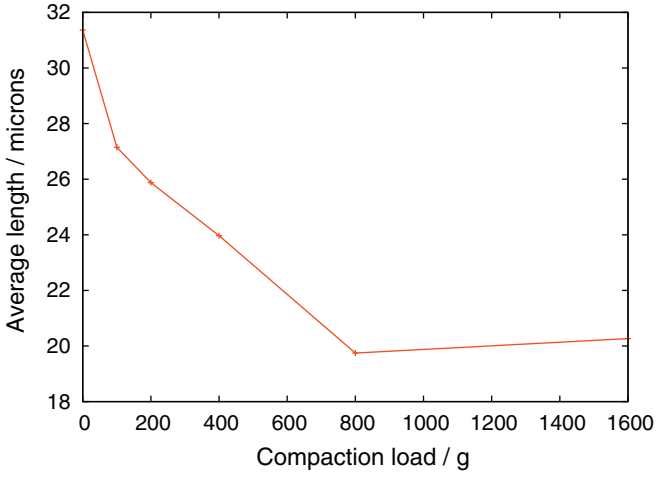

Fig. 10. Average particle size evaluated from experimental data.

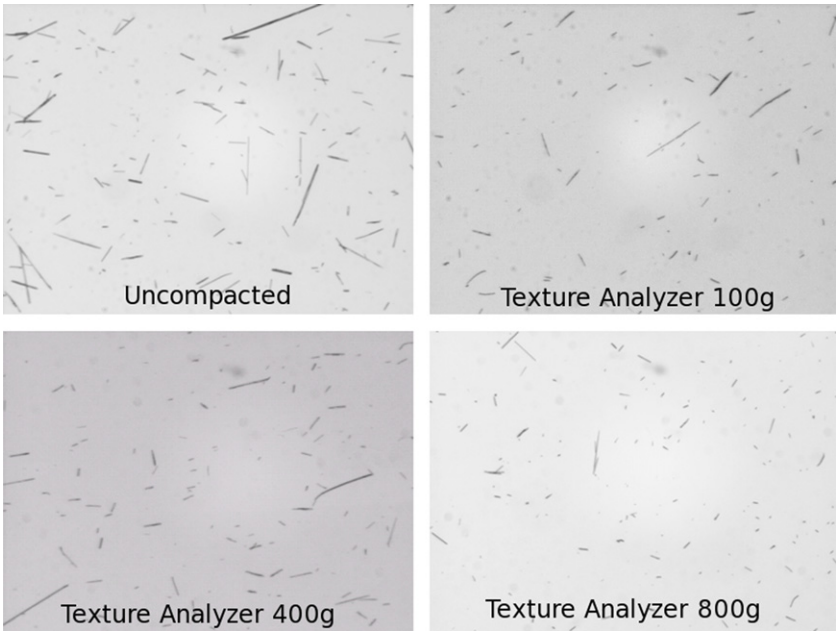

Fig. 8. Images of particles used for the evaluation of particle size distribution.

Table 2
Fitting of the experimental data by PBM.

Breakage kernel, $g(F)k(L_i)$	g(F)	c	k_0	γ	L_0	C	U
$g(F)(L_i - L_0)^\gamma$	Eq. (14)	3.90	0.0079	1.75	0	1.1	0.0793
$\frac{g(F)}{1+\exp(-\gamma(L_i - L_0))}$	Eq. (14)	10.5	0.81	0.75	4	1.2	0.0218

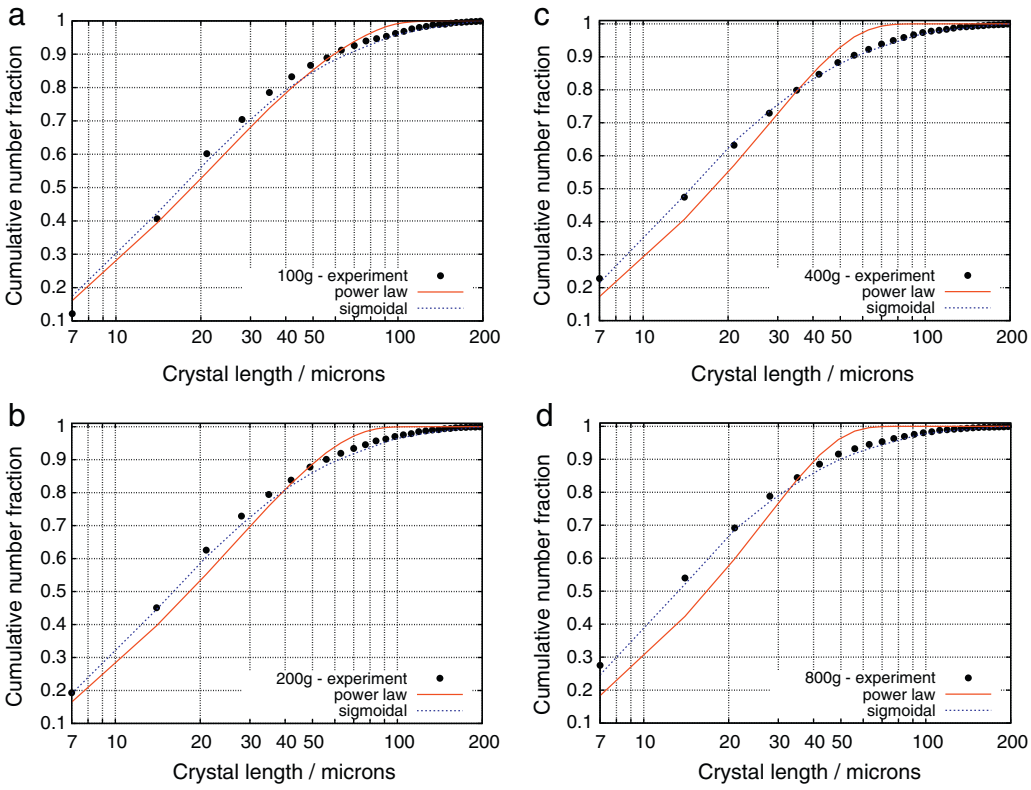

Fig. 11. Comparison of PBM with experiment.

be observed that particle size plateaus with increased compaction force, suggesting that the particles are no longer susceptible to uni-axial compaction breakage past a certain point.

6. Fitting of experimental results by PBM

The experimental data discussed in Section 5 were analyzed by the same optimization procedure that was used for the DEM data evaluation as described in Section 4. The population balance equations (15) with the compression force F as the independent variable were employed for the calculation of the number concentrations at different compressions.

After introducing the sigmoidal compression breakage kernels (24b) into the PB equations (15) with the compression force F as the independent variable, we obtain the following form of the population balance model for each size class i

$$\frac{dn_i}{dF} = k_0 \frac{2F + cF^2}{(1+cF)^2} \times \left(\frac{-n_i}{1+\exp(\gamma(L_i - L_0))} + \sum_{j=i+1}^{N} \frac{\beta_{ij} n_j}{1+\exp(\gamma(L_j - L_0))} \right). \quad (28)$$

The values of the optimum parameters and objective functions are compared in Table 2 and their graphical comparison with experimental data is shown in Fig. 11. In this case the fit is significantly better when employing the sigmoidal function. This can be explained by the particle size plateau at higher compaction forces (Fig. 10) suggesting that the particles are no longer breaking beyond a certain point and the corresponding breakage kernel indeed has a sigmoidal shape, as was observed also in the computational "experiments" by DEM.

7. Conclusions

It has been shown that computational and experimental techniques can be combined successfully into a single methodology that allows the identification of the breakage kernel and the daughter distribution functions for needle-shaped crystals, and of material-specific parameters appearing therein. A single-pass uni-axial compaction experiment has been shown to be sufficient, with no need for repeated differential breakage experiments. This approach can significantly reduce the experimental effort and therefore the time needed for the identification of the breakage kernel and daughter distribution functions and of material-specific parameters when the breakage properties of a new chemical entity (NCE) are to be determined. The approach combining modeling with experiment is particularly valuable in early-phase pharmaceutical process development when only small quantities of the NCE are often available and it is desirable to maximize the information gain from a limited number of experiments. By the combination of small-scale experimental analysis, population balance modeling, and DEM simulation, the information needed for the estimation of

in-process behavior of the powder can be obtained. Challenge areas for future research include the simulation of other modes of breakage – such as breakage under shear and breakage in the presence of capillary liquid bridges – as well as the integration of particle breakage models with large-scale CFD or DEM simulations of entire process vessels in order to predict the overall extent of breakage as a function of process-level parameters.

Acknowledgments

Financial support from the Czech Science Foundation (grant GA/104/08/P389) and the Czech Ministry of Education (project MSM 6046137306) is gratefully acknowledged.

References

Austin, L.G., 1971. Introduction to the mathematical description of grinding as a rate process. Powder Technol. 72, 1–17.
Bjorkmann, M., Holmstrom, K., 1999. Global optimization using the DIRECT algorithm in Matlab. Adv. Modell. Optimization 1, 17–36.
Bobet, A., Fakhimi, A., Johnson, S., Morris, J., Tonon, F., Yeung, R.M., 2009. Numerical models in discontinuous media: Review of advances for rock mechanics applications. J. Geotech. Geoenviron. Eng. 135, 1547–1561.
Cundall, P.A., Strack, O.D.L., 1979. A discrete numerical model for granular assemblies. Géotechnique 29, 47–65.
Favier, J.F., Abbaspour-Fard, M.H., Kremmer, M., Raji, A.O., 1999. Shape representation of axi-symmetrical, non-spherical particles in discrete element simulation using multi-element model particles. Eng. Comput. 16, 467–480.
Fuerstenau, D.W., Gutsche, O., Kapur, P.C., 1996. Confined particle bed comminution under compressive loads. Int. J. Miner. Process. 44-45, 521–537.
Fuerstenau, D.W., De, A., Kapur, P.C., 2004. Linear and nonlinear particle breakage processes in comminution systems. Int. J. Miner. Process. 74S, S317–S327.
Grof, Z., Kohout, M., Stepanek, F., 2007. Multi-scale simulation of needle-shaped particle breakage under uniaxial compaction. Chem. Eng. Sci. 62, 1418–1429.
Gupta, V.K., Hodouin, D., Berube, E.A., Everell, M.D., 1981. The estimation of rate and breakage distribution parameters from batch grinding data for a complex pyritic ore using a back-calculation method. Powder Technol. 28, 97–106.
Hill, P.J., Ng, K.M., 1997. Simulation of solids processes accounting for particle-size distribution. AIChE J. 43, 715–726.
Hill, P.J., 2004. Statistics of multiple particle breakage accounting for particle shape. AIChE J. 50, 937–952.
Kalman, H., 2000. Particle breakage and attrition. Kona 18, 108–120.
Kawakita, K., Lüdde, K.H., 1971. Some considerations on powder compression equations. Powder Technol. 4, 61–68.
Kelly, E.G., Spottiswood, D.J., 1990. The breakage function: what is it really? Minerals Eng. 3, 405–414.
Ketterhagen, W.R., am Ende, M.T., Hancock BC, 2008. Process modeling in the pharmaceutical industry using the discrete element method. J. Pharm. Sci. 98, 442–470.
Khanal, M., Schubert, W., Tomas, J., 2005. DEM simulation of diametrical compression test on particle compounds. Granul. Matter 7, 83–90.
Kostoglou, M., 2007. The linear breakage equation: from fundamental issues to numerical solution techniques. In: Salman, A.D., Ghadiri, M., Hounslow, M.J. (Eds.), Handbook of Powder Technology, vol. 12 – Particle Breakage. Elsevier, Amsterdam, pp. 793–835.
Müller, M., Meier, U., Wieckhusen, D., Beck, R., Pfeffer-Hennig, S., Schneeberger, R., 2006. Process development strategy to ascertain reproducible API polymorph manufacture. Cryst. Growth Des. 6, 946–954.
Perttunen, C.D., Jones, D.R., Stuckman, B.E., 1993. Lipschitzian optimization without the lipschitz constant. J. Optimiz. Theory App. 79, 157–181.
Rajniak, P., Dhanasekharan, K., Sinka, C., MacPhail, N., Chern, R., 2008. Modeling and measurement of granule attrition during pneumatic conveying in a laboratory scale system. Powder Technol. 185, 202–210.
Sathyagal, A.N., Ramkrishna, D., Narsimhan, G., 1995. Solutions of inverse problems in population balances: II. Particle break-up. Comput. Chem. Eng. 19, 437–451.
Vanni, M., 2000. Approximate population balance equations for aggregation-breakage processes. J. Colloid Interf. Sci. 221, 143–160.
Weichert, R., 1992. Application of defect statistics and fracture mechanics for describing comminution processes. Zement-Kalk-Gips Int. 3, 51–57.
Yu, Z.Q., Chew, J.W., Chow, P.S., Tan, R.B.H., 2007. Recent advances in crystallization control: an industrial perspective. Chem. Eng. Res. Des. 85 (A7), 893–905.